Available online at www.sciencedirect.com
ScienceDirect
Journal of the European Ceramic Society 32 (2012) 123–132
www.elsevier.com/locate/jeurceramsoc

Spherical instrumented indentation of porous nanocrystalline zirconia

R.K. Chintapalli [a], E. Jimenez-Pique [a,b], F.G. Marro [a,b], H. Yan [c,d], M. Reece [c,d], M. Anglada [a,*]

[a] Department of Materials Science and Metallurgical Engineering, Universitat Politecnica de Catalunya 647, Av Diagonal, Barcelona 08028, Spain
[b] Center for Research in Nanoengineering, CRnE, Universitat Politècncica de Catalunya, Spain
[c] School of Engineering and Materials Science, Queen Mary College, University of London, Mile End Road, London E1 4NS, UK
[d] Nanoforce Technology Ltd, Mile End Rd, London E1 4NS, UK

Received 30 May 2011; received in revised form 19 July 2011; accepted 24 July 2011
Available online 8 September 2011

Abstract

Nanoindentation tests with a spherical tip were performed to analyze the stress–strain response on 3-mol%-yttria-doped tetragonal zirconia polycrystals produced by spark plasma sintering (SPS) with porosities in the range 2–21% and nanometric average grain sizes in the range 65–120 nm. Indentation stress–strain curves were obtained by using load (P)–displacement (h) data. Onset of elasto-plastic transition was determined by Hertz fits on P–h curves. Elastic modulus obtained from spherical indentation was similar to the values obtained by Berkovich indentation, with a slight difference with increasing porosity. Microstructural characterisation shows no cracks around and beneath the indentations. Raman spectroscopic analysis of the residual indentation imprints reveals tetragonal to monoclinic phase transformation in the most porous material, whereas no phase transformation was detected in the dense material in spite of its larger grain size. The results are discussed in terms of porosity, grain size and tetragonal-monoclinic transformability.

Keywords: Zirconia; Sintering; Porosity; Grain size; Mechanical properties

1. Introduction

Porous zirconia ceramics are attractive candidates for a wide array of applications such as prosthetics, dentistry, environmental filters, and sensors[1–3] among other applications. Additionally, porous zirconia ceramics are highly regarded materials as bone scaffolds coated with hydroxyapatite (HA),[4,5] where zirconia is used as a load bearing component and the HA coating is for promoting bioactivity. For load bearing applications, the capacity of the material to absorb energy and sustain the deformation becomes critical, so that mechanical properties such as stress–strain behaviour and yield strength are of great interest in order to assess the material deformation behaviour.

Given the quasi-plastic nature of zirconia ceramics, it is important to quantify the deformation and yield behaviour as these properties are critical in applications where the material is under contact loading. Indentation studies are commonly used for characterising fracture and deformation behaviour of brittle ceramics; more specifically, contact damage is analyzed by Hertzian testing using spherical indenters.[6,7] On the other hand, the influence of porosity on indentation stress–strain behaviour and contact damage response has severe implications concerning the capacity of ceramics to sustain mechanical damage and for improving reliability.[8]

Tetragonal polycrystalline zirconia doped with 3% molar yttria (3Y-TZP) with typical average grain size around 300 nm and density close to theoretical density, as well as zirconia ceramics doped with Mg or Ce, have been studied by using indentation in order to assess their deformation behaviour.[9–12] Indentation damage mechanisms have been discussed in a review article by Lawn[13] on spherical indentation of ceramics.

Nanoindentation with sharp indenters has also been used in conventional 3Y-TZP to determine contact hardness and elastic modulus.[14,15] By contrast, to the best of our knowledge, there is a lack of information on the influence of nanometric grain size and porosity on the indentation stress–strain behaviour and yielding. The aim of the present study is to explore these points by using spherical nanoindentation in 3Y-TZP produced by spark plasma sintering with nanometric grain size, in which porosity is present in a variable degree.

* Corresponding author. Tel.: +34 93 40 16701.
E-mail address: marc.j.anglada@upc.edu (M. Anglada).

0955-2219/$ – see front matter © 2011 Elsevier Ltd. All rights reserved.
doi:10.1016/j.jeurceramsoc.2011.07.037

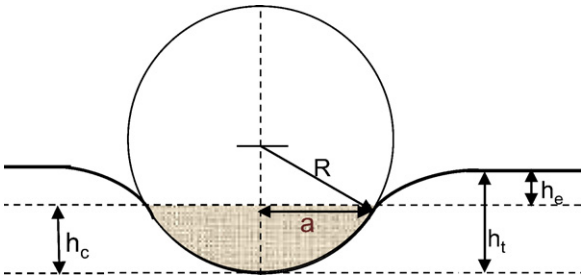

Fig. 1. Schematic representation of spherical indentation.

Nanoindentation is a powerful technique for measuring mechanical properties with high resolution, which allows measuring properties at the micro-nano scale.[16] This technique is based on the analysis of the indentation load–displacement curves. The response of the material to contact loading will depend on the geometry of indenter used, which generally are sharp or blunt indenters. Sharp indenters produce an elasto-plastic response from the beginning of the indentation. Blunt indenters, on the other hand, produce an elastic contact during initial loading and can be used to observe the elastic behaviour as well as the elasto-plastic transition, which cannot be obtained directly by sharp indentation.[17,18] Additionally, spherical indentations permit to probe larger volumes of material at the beginning of the contact, and therefore are less sensitive to heterogeneities in the material.

Several methods have been proposed[19,20] for determining the mechanical properties by using instrumented spherical indentation and for converting the data into stress–strain curves.[21–24] In the present work the CSM (continuous stiffness measurement) technique was used to measure the contact stiffness for all further analysis of the indentation data. The indentation stress–strain curves and yield points of 3Y-TZP with different porosity and grain sizes are presented and possible damage mechanisms are discussed.

1.1. Theoretical model for spherical indentation

Fig. 1 schematically represents the interaction between a flat surface and a spherical indenter. The response of the sample plus indenter under spherical indentation is divided into elastic and elasto-plastic regimes. The elastic regime can be described by Hertz equations for small penetration depths[19,25,26]:

$$P = \frac{3}{4} E_{\text{eff}} \sqrt{R} {h_t}^{3/2} \tag{1}$$

$$\frac{1}{E_{\text{eff}}} = \frac{1-\nu^2}{E} + \frac{1-\nu'^2}{E'} \tag{2}$$

where P is the applied load, R is the indenter radius, h_t is the total displacement into the surface, E_{eff} is the effective modulus of indenter-sample system, E and E' are the elastic modulus of sample and indenter respectively. For a spherical indenter, Sneddon[27] demonstrated that the elastic displacement is related to the contact radius a as:

$$h_e = h_{\text{total}} = \frac{a^2}{R} \tag{3}$$

Substituting Eq. (3) in Eq. (1) yields:

$$\frac{P}{\pi a^2} = \frac{4}{3\pi} E_{\text{eff}} \left(\frac{a}{R}\right) \tag{4}$$

The left-hand side of Eq. (4) is the Meyer hardness, represented as indentation stress and the parenthesis on the right-hand side stands for indentation strain.[25] During a nanoindentation test, load–displacement data and contact stiffness (from the CSM module) are recorded. In particular, the contact depth is calculated from the direct stiffness measurement, S, for the elasto-plastic regime as[26]:

$$h_c = h_t - \frac{3P}{4S} \tag{5}$$

Then the contact radius can be calculated as:

$$a = \sqrt{2Rh_c - h_c^2} \tag{6}$$

Therefore, the nanoindentation test allows calculating the contact radius a using Eq. (6). Then, it is possible to obtain the indentation stress $P/\pi a^2$ and the indentation strain a/R. Additionally, it has been shown[28] that for an isotropic material indented with a sphere, the contact stiffness is proportional to the contact radius. This linear dependency was used in the present work for tip calibration and to correct the zero contact point:

$$S = 2E_{\text{eff}} a \tag{7}$$

2. Material and methods

Commercially available zirconia powder (TZ-3YSB-E, Tosoh Co, Japan) with 3% molar of yttria was used to prepare the samples. The powder was preheated to 750 °C and then introduced in a graphite die and sintered by spark plasma sintering (SPS FCT HP D25I, FCT system GmBh). Samples were sintered at three different temperatures under a pressure of 100 MPa for a dwell time of 5 min. Discs of 20 mm diameter and 4 mm in thickness were produced. Bulk density and apparent porosity were measured according to the ASTM standard C 20-00[29] and the results are shown in Table 1. Samples were then ground and polished in different steps using 30, 6 and 3 μm diamond paste and finally with 0.03 μm colloidal silica. Surface roughness (R_a) measured with a profilometer was in the range of 0.02–0.06 μm for the dense and the porous materials. Samples were labelled after their apparent porosity as Zr21, Zr9 and Zr2, which correspond to increasing sintering temperatures. Porosity area fraction, average pore size, and mean grain sizes were measured from SEM images by using Buehler OMNIMET 5.4 image analysis software and the results are shown in Table 2. Hardness (HV1) of all samples was measured using a Vickers indenter by applying a load of 1 kg.

Table 1
Sintering temperature and physical properties.

Material	Sintering temperature (°C)	Bulk density (g/cm^3)	Relative density (%)	Apparent porosity (%)	Open porosity (%)	Closed porosity (%)
Zr-21	1100	4.79	78.52	21.26	4.52	16.74
Zr-9	1150	5.49	90.01	9.36	0.41	8.95
Zr-2	1175	5.98	98.03	1.91	–	–

Note: Theoretical density of 3Y-TZP is 6.1 g/cm^3.

Nanoindentations were made with an MTS Nanoindenter XP equipped with a CSM module. A diamond spherical indenter tip with a nominal radius of 25 μm was used. Indentations were made to a maximum depth of 2000 nm and under a constant deformation rate of 0.05 s^{-1}. Arrays of 4 by 4 indentations were carried out in each material with an inter-indentation spacing of 50 μm. About 1200 data points (load, displacement, stiffness and time) were collected for each indentation. At maximum penetration, the contact area was very large in comparison with the pore size and the average distance between pores, so that for each material the measured elastic modulus and hardness did not change significantly with the position of the indenter. Additionally, contact hardness and elastic modulus were determined by nanoindentation with a Berkovich tip up to 630 mN load. Both spherical and Berkovich tips were calibrated against a standard fused silica. The spherical nanoindentation imprints were later observed by an atomic force microscope (AFM Dimension Veeco Inc.) in tapping mode.

A triple monochromator spectrometer (T64000 Horiba/Jobin–Yvon) with a coupled CCD detector (liquid nitrogen cooled) was used to obtain Raman spectra on the residual indentation imprints. An Ar-ion laser Innova 300 (Coherent Laser Group) was used as a light source and excited at a wavelength of 514 nm. Raman spectra were collected from the centre and the border of the indent at 100× magnification with a lateral resolution of 1 μm, and the spectrum integration time was 60 s, with the recorded spectra averaged over four successive measurements. The sampling depth of the laser for Raman spectroscopy was approximately 40 μm below the surface.[15]

Focused Ion Beam (FIB) cross sections were performed in a Zeiss Neon 40 microscope. A platinum layer was deposited before milling to protect the material. Trenches were milled with decreasing Ga^+ currents at 30 kV down to 100 pA. Some curtain effect appears in the pictures due to the interaction of the porosity with the ion beam.

Table 2
Measurements of porosity and grain sizes.

Material	Porosity area fraction (%)	Average pore size (μm)	Mean grain size (nm)
Zr-21	29.56 ± 2.95	0.24 ± 0.13	65 ± 20
Zr-9	11.19 ± 1.16	0.14 ± 0.09	90 ± 30
Zr-2	–	–	120 ± 20

3. Results

3.1. Tip calibration

In order to check the correct calibration of the tip, tests were firstly done on fused silica as a reference material. Fig. 2(i) shows the obtained *P–h* curve, where it can be seen that the unloading curve overlaps the loading curve, indicating that the deformation is elastic. Fig. 2(ii) shows the h_c vs *a* curve which reflects the tip shape. From the known elastic modulus of fused silica and using Eqs. (2), (6) and (7), the tip radius is calculated as 23.9 ± 0.4 μm for depths equal or less than 1200 nm, which is close to the nominal tip radius of 25 μm.

3.2. Porosity

Table 2 displays the resulting microstructural parameters measured on SEM micrographs. Fig. 3 shows the microstruc-

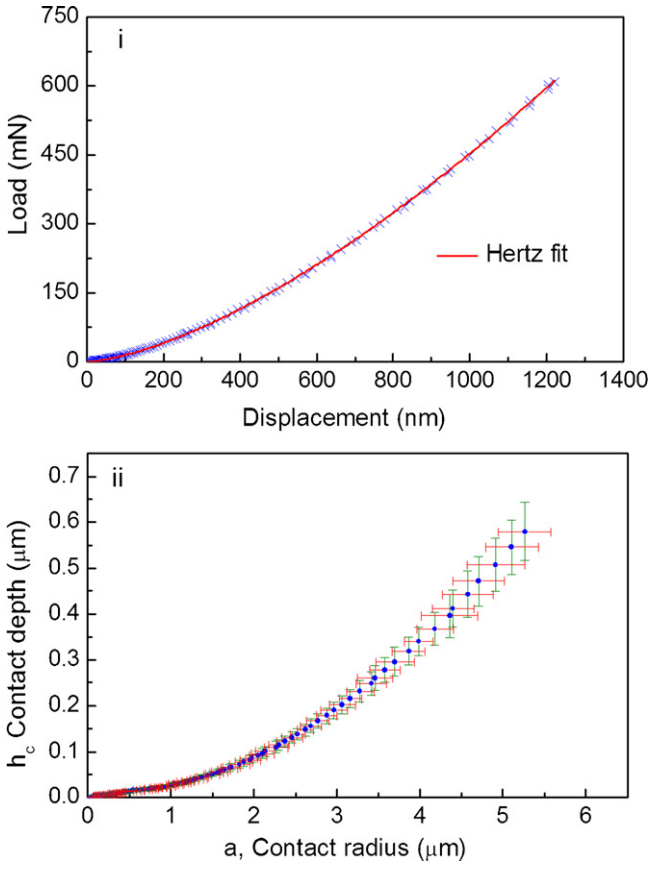

Fig. 2. (i) *P–h* curve for fused silica (ii) h_c vs *a*, for spherical indentation on fused silica.

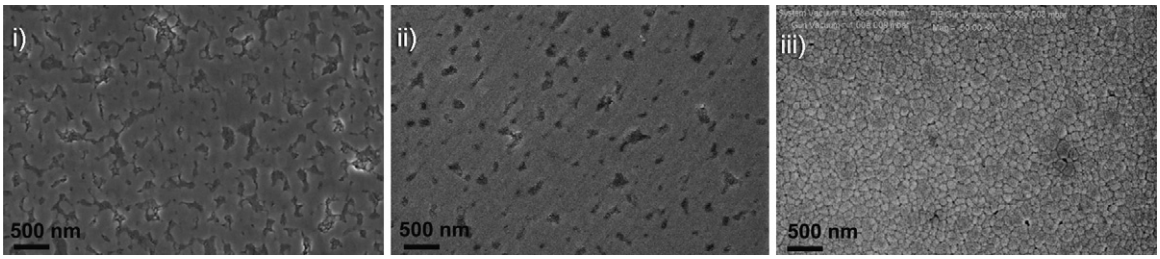

Fig. 3. SEM micrographs of (i) Zr21, (ii) Zr9 and (iii) Zr2.

tures of all materials. It can observed from Fig. 3 that in Zr21 pores are interconnected and elongated, in Zr9 they are closed and nearly having spherical shape, while in Zr2 very few pores were present. It is clear that pores become increasingly irregular in shape with the increase of porosity which corresponds to the decrease in sintering temperature. This non-uniformity arises from the sintering process which depends on dwell time, temperature, and pressure applied and release conditions during spark plasma sintering. This leads to incomplete densification leaving the inhomogeneous submicron undensified zones in the material.

3.3. Determination of contact point

At reduced length scales, determining the initial contact point where load and displacement are zero is the key to plot the correct material response. The contact point in nanoindentation, especially with tips with a large radius of curvature, may be incorrectly determined due to surface-tip interactions, such as capillary forces or electrostatic interactions. Several different methods to determine the contact point have been discussed in literature.[30–33] Moseson et al.[33] used the S vs. a relationship (Eq. (7)) to fit the curve through the origin and correct the contact point. Fig. 4 (inset) shows the raw stiffness vs. contact radius; here the apparent lack of linearity is clearly visible. A linear regression analysis was performed in the apparent linear part of the curves and the contact point was found by extrapolation to zero, as shown in Fig. 4. The plot of S vs. a in all the range studied shows a linear tendency with a slope corresponding to $2E_{\text{eff}}$, which is also an indication that contact stiffness S was not affected by the plastic deformation.[21]

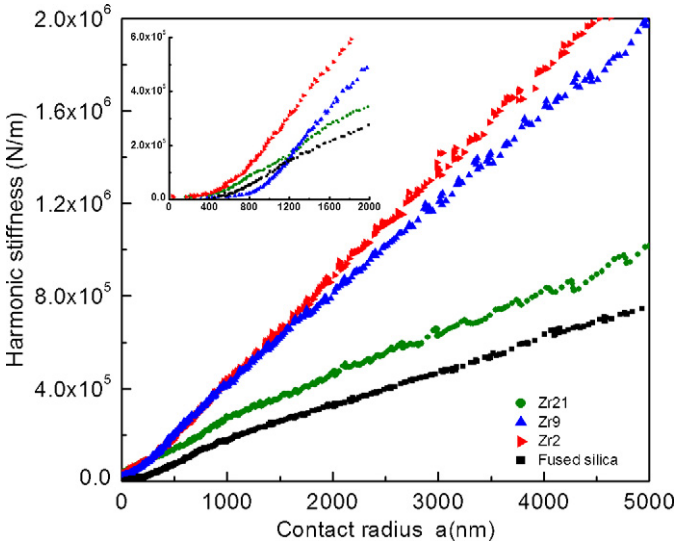

Fig. 4. Stiffness against contact radius and raw data before correction (inset).

3.4. Load–displacement curves

Fig. 5 shows the sample load–displacement curves for the three materials. The indentations were force-controlled until a maximum penetration depth of 2 μm was reached. The maximum load, $P_{\max}$, in each material was 1, 2.4, and 3 N for Zr21, Zr9 and Zr2, respectively. The solid line represents the Hertzian fit according to Eq. (1) by considering the determined spherical nanoindentation modulus; details of how the elastic modulus is obtained are given in next section. Fig. 5 displays the initial loading part of the curves, which can be satisfactorily fitted with Hertz equations. Deviations from Hertz curve are attributed to yielding, that is, the onset of elasto-plastic deformation in all samples. At this stage, deformation is controlled by both elastic and plastic processes. In each sample, yielding occurs at different load and displacement due to the microstructural dissimilarities and/or porosity in the samples. For instance, in the porous Zr21, elasto-plastic response starts around ~100 mN load and a depth of ~350 nm, whereas in the dense Zr2 it occurs around ~400 mN load and a depth of ~450 nm. Fig. 5(iv) shows a comparison of the load–unloading curve for the three materials with different porosity. The load required for penetration depths up to ~2 μm is decreasing with increasing porosity. The area between the load and unloading curves describes the amount of irreversible deformation. The large area in Zr21 is attributed to the large plastic response and low elastic recovery, and in Zr2 the small area is due to small plastic response and high elastic recovery.

3.5. Indentation stress–strain curves

Fig. 6 illustrates the indentation stress–strain curves for the different materials. These curves are the average for all indentations for each material and are presented with standard deviation in both stress and strain. In spite of porosity, the curves for Zr21 and Zr9 exhibit low standard deviation in the elastic region, but slight increase was observed after yielding. The increase in the scatter in the elasto-plastic regime is believed to be caused by the local inhomogeneties in porosity beneath each indentation and/or associated deformation events. The dashed line is the fit obtained by using linear regression analysis of the elastic part of

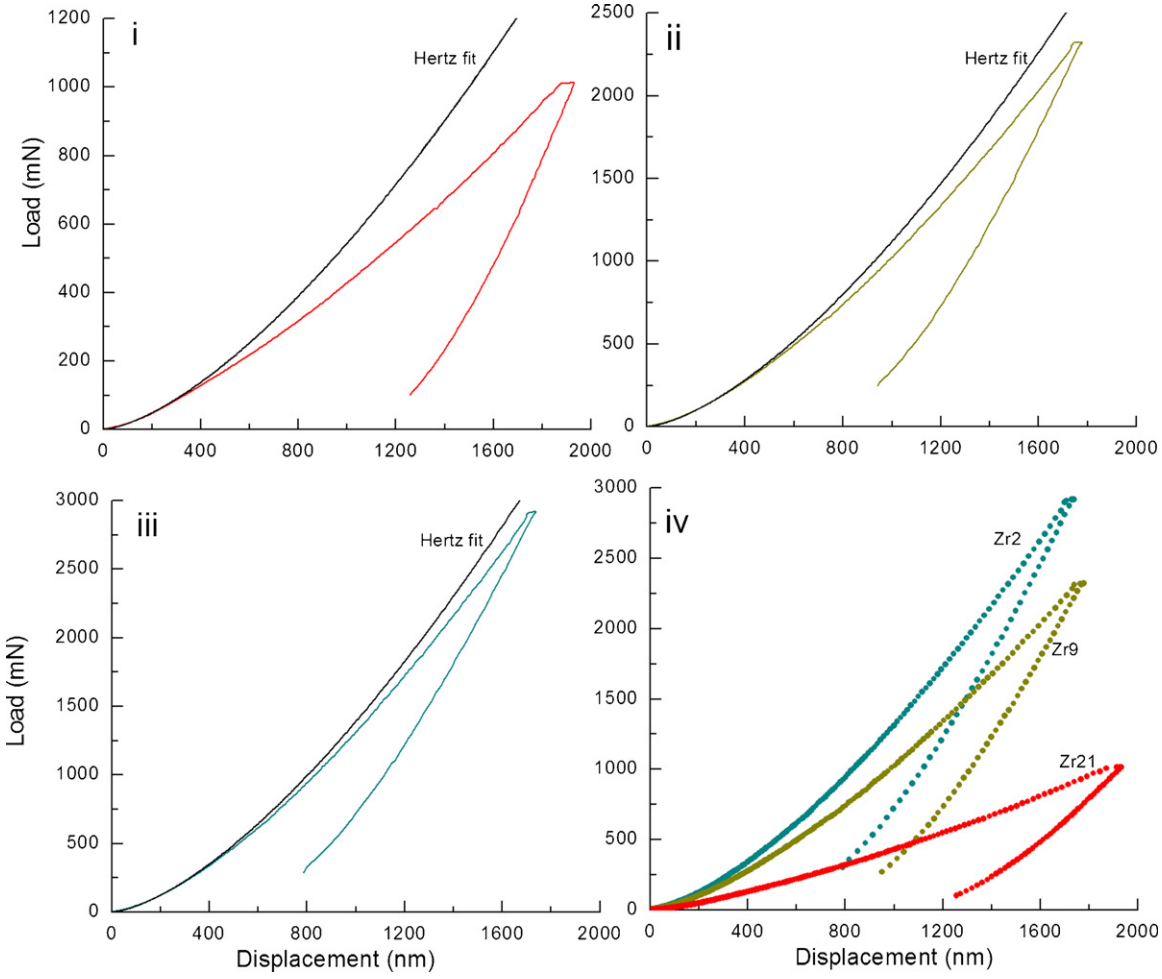

Fig. 5. *P–h* curves with Hertz fit of (i) Zr21, (ii) Zr9, (iii) Zr2, and (iv) comparison of the three materials.

the curve. The elastic moduli were determined from this slope and are presented in Table 3. Pop-in events (sudden discontinuities in displacement due to cracking and other deformation mechanisms) were not observed in the *P–h* curves. Therefore, yield strength is obtained from the corresponding deviation point of the Hertz fit of the load–displacement curve. The average yield strength for all indentations together with the standard deviation is given in Table 3.

Repeatability of the material behaviour under indentation was not affected by the porosity because of very small pore size ~0.24 μm compared to the contact radius. This is because the used contact stiffness for determining the point of contact by extrapolation from the linear behaviour, were selected from measurements with a relative large contact radius of at least ~2 μm. Therefore many pores were pressed in the volume affected by the contact during each indentation.

It can be observed that the indentation stress required for yielding decreases with increasing porosity. After yielding, the apparent stress required to cause further deformation increases in all materials. The elasto-plastic transition is clearly observed in Zr21 and Zr9, where in the case of Zr2, the deviation of stress–strain curve from elastic line is less abrupt, and is closer to the elastic trend. Spherical indentation modulus (E_{Sph}) is similar to the values obtained by Berkovich nanoindentation (E_{Ber}), except in the case of Zr21. The cause of this discrepancy is discussed later.

Table 3
Elastic modulus, hardness and yield strength.

Material	Fused silica	Zr21	Zr9	Zr2	Ref. 39
$Hardness_{Ber}$ (GPa)	9.5 ± 0.5	6.5 ± 1.9	12.5 ± 1.8	17.2 ± 2.4	17.5
Hardness (HV) (GPa)	–	6.2 ± 0.5	11.4 ± 0.3	14.5 ± 0.2	–
Yield stress, σ_y (GPa)	–	2.1 ± 0.3	6.7 ± 0.2	9.4 ± 0.4	–
$Elastic\ modulus_{Ber}$ (GPa)	72 ± 1	121 ± 5	200 ± 7	230 ± 3	250
$Elastic\ modulus_{Sph}$ (GPa)	70 ± 2	89 ± 8	181 ± 6	223 ± 4	–

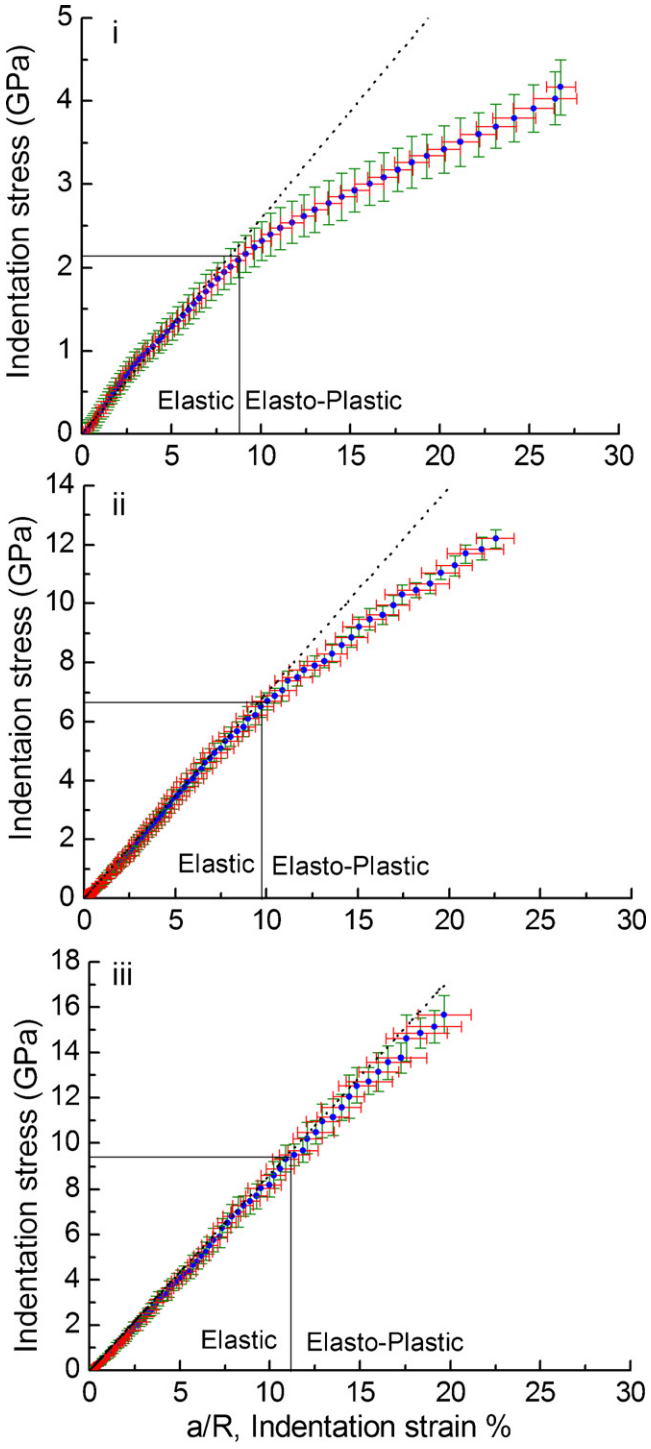

Fig. 6. Indentation stress–strain curves of (i) Zr21, (ii) Zr9, and (iii) Zr2.

3.6. Damage characterisation

Residual indentation imprints and depth profiles of the spherical indentations are displayed in Fig. 8. Permanent deformations on the surface without any cracks were observed in all samples. Residual indentation depths ranged from ~0.85 to ~0.25 μm for Zr21 to Zr2 respectively. The indentation profiles (see Fig. 7(iv)) show no significant pileup around the indentations. Additionally, the imprints were larger on the more porous materials.

Phase transformation was then locally analyzed by micro-Raman spectroscopy on the nanoindentation imprints. Fig. 8 shows the spectra obtained in the centre and border of the imprints, with the peaks labelled with the respective phase (t – tetragonal, m – monoclinic). Additionally a spectrum obtained from 2 mm away from the indentations indicates that the material has tetragonal phase. In Zr21, a clear phase transformation from tetragonal to monoclinic was observed at the centre and border of the indentation. In Zr9 and Zr2, very low and no phase transformation, respectively, was detected. All spectra are fitted with Lorentzian functions on a linear background[34] for quantification of monoclinic phase. Monoclinic volume fraction was quantified using the model proposed by Katagiri et al.[35] and it is found to be $17 \pm 2\%$ in Zr21. Quantifying monoclinic volume fraction in Zr9 is complex due to the low amount of transformation (less than 7%).

Focused ion-beam (FIB) cross-sections were prepared on indention impressions in all materials. The FIB cut was made from the centre of indentations. Sample surfaces were previously protected with thin platinum coating for ion milling. Fig. 9 shows the SEM images of cross-sections of indentations. In porous materials, curtain effect can be observed due to the porosity and the large cut area. The indentation imprint profile is highlighted with a dashed line. In Zr21, the porosity is highly irregular and often interconnected and the region under the indentation shows some indication of compaction. High magnification views of the dashed rectangles from Fig. 9(i) are shown in Fig. 10 with the respective zones marked as 1 and 2. The main difference in zone 1 and zone 2 is that considerable shrinkage in pores is clearly seen in zone 1, which is not the case in zone 2. Also it appears that in zone 1, some pores are closed forming a crack like appearance, which are indicated by arrows. But with a clear observation one can realise that these crack like lines are in fact formed by pore faces which came together partially under the load. In Zr9, the porosity is dispersed and the interaction between the pores is minimal. In all materials, irrespective of porosity, no cracks were observed under the indentations.

4. Discussion

The spherical tip radius is believed to be constant in spherical indentation analysis; however it has been previously reported that the tip radius changes with depth.[22,36] In this work, spherical indentation on a standard fused silica produced only elastic deformation (see Fig. 2) within a penetration depth of 1200 nm. Moreover, the indentation yield points in the studied materials were between 350 and 450 nm, which is well below the test range analyzed for fused silica. It can be observed in Table 3 that the values found for spherical and Berkovich indentation elastic moduli of fused silica are quite similar. They are also close to the standard value for fused silica so that it is justified the validity of the tip radius for the spherical indenter within the test range.

The elastic properties of porous ceramics depend of many factors like total porosity and shape of the pores and of the solid phase, but no universal model exists to describe the elastic modulus.[37] One simple empirical equation for the elastic modu-

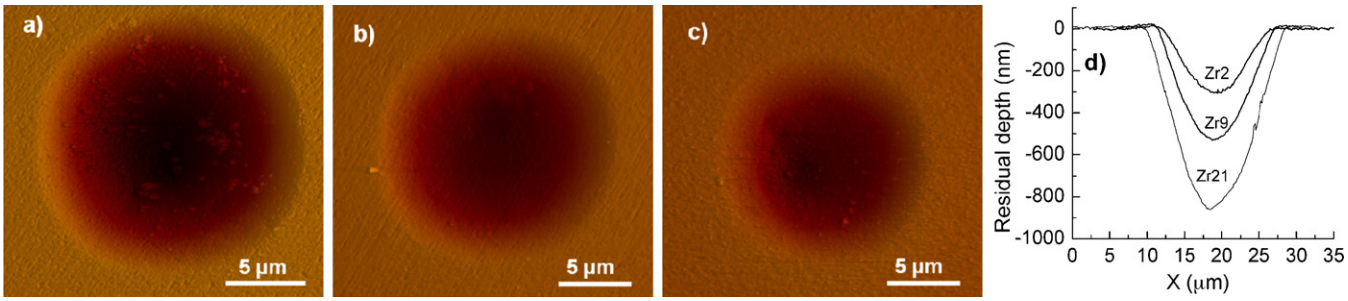

Fig. 7. AFM tapping mode height images showing residual spherical indentation imprint on (a) Zr21 at 1 N, (b) Zr9 at 2.4 N, (c) Zr2 at 2.9 N load and (d) residual depth profiles.

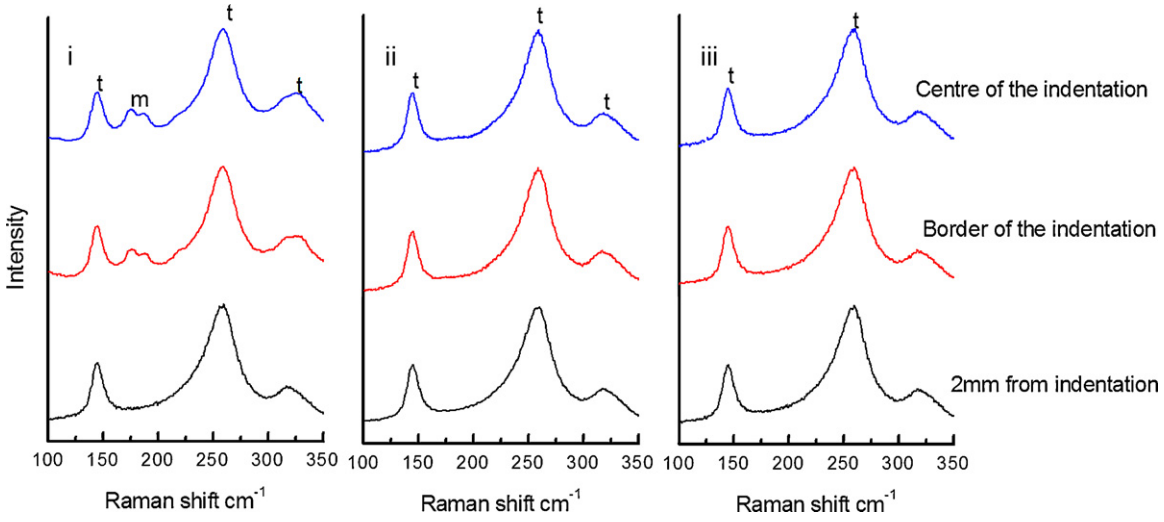

Fig. 8. Micro Raman spectra of the residual indentation imprints of (i) Zr21, (ii) Zr9 and (iii) Zr2.

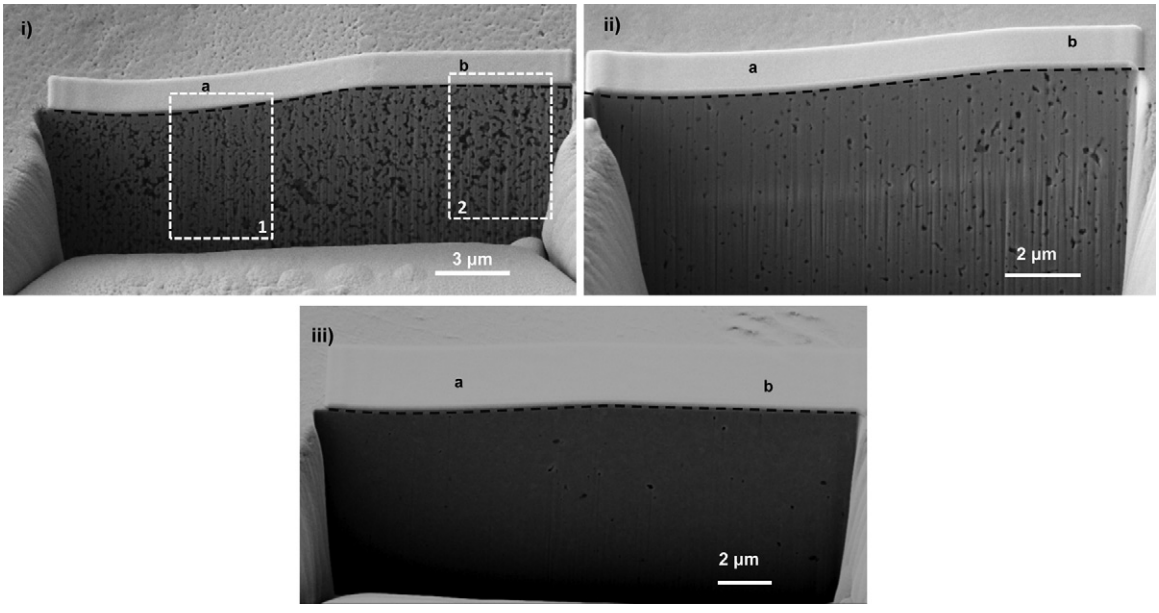

Fig. 9. SEM micrographs of FIB cross-sections of spherical indentation (i) Zr21, (ii) Zr9 and (iii) Zr2. Notations *a* and *b* are the locations of indentation and surface, respectively.

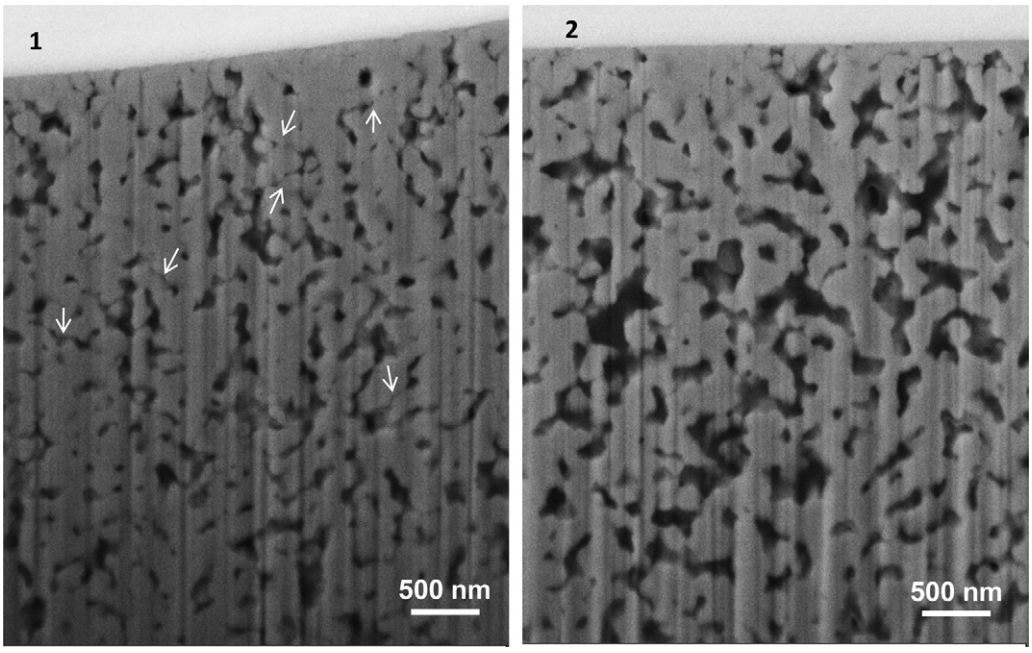

Fig. 10. High magnification views of marked zones in Fig. 9(i).

lus with a fitting parameter which can be related to the shape of pores was used by Luo and Steven[38] in conventionally sintered 3Y-TZP and it can be expressed as

$$E = E_0 \frac{1 - P}{1 + \alpha P} \tag{8}$$

E_0 corresponds to the elastic modulus of a pore-free material (230 GPa) and P is the porosity volume fraction. The parameter α has been related to the shape of the pores in 3Y-TZP[38]; for spherical pores it has a value close to 1 and increases as the spherical pores change to oblate spheroids. In the present case, the values of α for fitting our measurements of the elastic modulus by spherical indentation are approximately 1 for $P = 0.02$ and 0.09, and 5 for $P = 0.21$ (see Fig. 11).

In Zr21, the intersection of pores is significant (see Fig. 3i), so that actually the effective shape of the pores change; they appear to be elongated and often interconnected. If we assume they are spheroids, the average ratio between their radii (β) is about 0.02. On the other hand, in Zr9 most of the pores have near spherical shape and are dispersed with β close to the unity (0.86). Due to this sharp contrast between the pore shape in Zr21 and Zr9, the constant α in Eq. (8) for fitting should be different. It can be seen that $\alpha = 1$ for Zr9 is in full agreement with the measured pore shape ($\beta \sim 0.86$), but in Zr21 we find $a = 5$ and this value corresponds to spheroids that are more oblate ($\beta \sim 0.1$) than those measured ($\beta \sim 0.2$). However, the result is consistent with oblate spheroids and one has to take into account that porosity in Zr21 is interconnected, which is not taken into account in the model.

The values of hardness and yield strength decrease, as expected, with porosity. Their reduction follows a similar trend as the elastic modulus in the sense that they show a sharp reduction of properties in Zr21, which is attributed not only to the increase in porosity but also to the pore shape and to its interconnected character.

The discrepancy between the elastic modulus measured by Berkovich and spherical indentation is higher with increasing porosity. In the dense sample Zr2, the elastic moduli measured by both techniques are similar. The values of the elastic modulus determined by spherical indentation are more representative of the actual porosity than those measured by using a Berkovich indenter. This is related to the indenter tip shape and the fact that the modulus in spherical indentation is obtained from fitting the elastic part of the stress–strain curve. In sharp indentation, plastic deformation is produced from the initial contact which results in

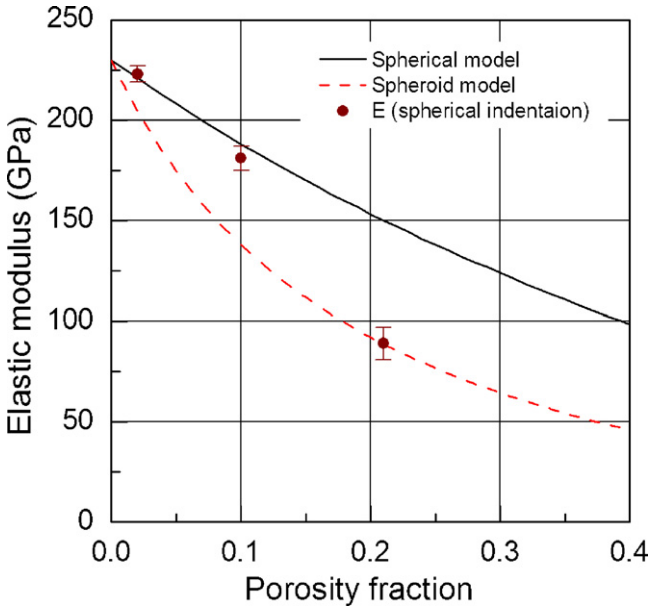

Fig. 11. Effect of pore shape and porosity content on elastic modulus.

partial closure of pores and densification; but beneath the spherical indenter, where the elastic–plastic transition is produced at relatively high loads, the pore structure will be more intact during the initial contact loads, and, therefore, the spherical elastic modulus will be lower than in sharp indentation.

Gaillard et al.[39] studied nanoindentation behaviour of fully dense 3Y-TZP of larger grain size (300 nm) under sharp indentation. They observed pile up around the indentation, which was attributed to the increase in volume by phase transformation. In the same work,[39] but under spherical indentation, phase transformation was clearly observed at 2.7 N with a similar indenter to that used here. In our results for Zr2 of lower grain size (120 nm), no phase transformation was detected at 2.9 N with the same indenter radius. This can be attributed to the smaller grain size that precludes tetragonal – monoclinic transformation under contact loading. The tetragonal phase can remain stable when the grain size is below a critical value, since the activation barrier for *t–m* transformation increases when the size of the critical nucleus decreases.[40,41] Along the same lines, it is interesting to notice that the three materials studied do not suffer low temperature degradation,[42] presumably because the stresses produced during hydrothermal ageing are not large enough to activate *t–m* transformation in the present nanometric grain sizes.

The fact that in the more porous material transformation is observed under a load below 2.7 N, suggests that porosity has a clear effect on phase transformation. The latter is associated with a volume expansion in 3Y-TZP, which is seen as a pileup around the indentation in dense zirconia of micrometric grain size. However, since in Zr21 pileup was not observed in spite of the presence of phase transformation as detected by Raman analysis, it is suggested that the increase in volume due to phase transformation has been accommodated by neighbouring porosity. It is well known that *t–m* transformation with its associated volume expansion is easier when tensile and shear stresses are high and the volume expansion is not constrained. The presence of large amount of porosity decreases the average components of the stress but not necessarily the local stresses and reduces the constraint for volume expansion. The stress distribution is a critical factor for transformation,[43] stresses with the same sign as the component of transformation tensor are known to assist transformation, so that shear and tensile are destabilizing, whereas compression are stabilizing.[44–46] In case of dense material (Zr2) the volume in contact with the indenter is experiencing homogeneous higher compression stresses, but the material below the indentation is highly constrained. In the more porous material (Zr21) the average components of the stress are smaller, but they change locally and may reach high values at the same time that the constraint by the surrounding material is much less due to the porosity. The fact that phase transformation acts as toughening mechanism in zirconia ceramics could be beneficial in case of nanocrystalline porous zirconia for resistance to surface damage.

5. Conclusions

Spherical nanoindentations were made on porous nanocrystalline zirconia produced by SPS. The stress–strain curves and indentation yield strength were obtained. Additionally, elastic modulus was obtained and compared with that of sharp indentation. Damage due to indentation was analyzed on the surface and beneath. Results are summarised as follows:

i. Mechanical properties such as elastic modulus, hardness and indentation yield strength were affected by the porosity. Once the porosity becomes interconnected the decrease in mechanical properties is more dramatic.
ii. Spherical indentation elastic modulus is comparable to that of the Berkovich indentation modulus in all materials except for a slight difference in the most porous material; this is attributed to the densification during the Berkovich indentation.
iii. No transformation is found in the dense nanometric materials under spherical contact loading. However, the presence of significant porosity promotes *t–m* phase transformation under the indentation because of high local effective shear stresses and reduction of constraint for volume expansion close to the pores.

Acknowledgements

The authors greatly acknowledge the financial support from the Ministerio de Ciencia e Innovación (MICINN) of Spain through project MAT2008-03398 and the partial grant given to F. Garcia Marro. The general financial support to the research group given by the Generalitat de Catalunya is also acknowledged (2009SGR01285). RKC is fellow of MAEC-AECID and expresses his gratitude to Ministerio de Asuntos Exteriores y de Cooperación. Finally, the authors would like to thank Dr. A. Mestra for his help in Raman experiments and Dr. Trifon Trifonov for his help in making FIB trenches.

References

1. Maca K, Dobsak P, Boccaccini AR. Fabrication of graded porous ceramics using alumina–carbon powder mixtures. *Ceram Int* 2001;**27**:577–84.
2. Biasini V, Parasporo M, Bellosi A. Fabrication and characterisation of Al_2O_3 porous bodies by hot isostatic pressing. *Thin Solid Film* 1997;**297**:207–11.
3. Gain AK, Song HY, Lee BT. Microstructure and mechanical properties of porous yttria stabilized zirconia ceramic using poly methyl methacrylate powder. *Scripta Mater* 2006;**54**:2081–5.
4. Miao X, Hu Y, Liu J, Huang X. Hydroxyapatite coating on porous zirconia. *Mater Sci Eng C* 2007;**27**:257–61.
5. Kim HW, Lee SY, Bae CJ, Noh YJ, Kim HE, Kim HM, et al. Porous ZrO_2 bone scaffold coated with hydroxyapatite with fluorapatite intermediate layer. *Biomaterials* 2003;**24**:3277–84.
6. Lawn BR, Wilshaw TR. Indentation fracture: principles and applications. *Mater Sci* 1975;**10**(6):1049–81.
7. Lawn BR. Fracture of brittle solids. Cambridge, UK: Cambridge University Press; 1993.
8. Latella BA, OConnor BH, Padture NP, Lawn BR. Hertzian contact damage in porous alumina ceramics. *J Am Ceram Soc* 1997;**80**(4):1027–31.
9. Suganuma M. Spherical and vickers indentation damage in yttria-stabilized tetragonal zirconia polycrystals. *J Am Ceram Soc* 1999;**82**:3113–20.
10. Kun LS, Tandon R, Readey MJ, Lawn BR. Scratch damage in zirconia ceramics. *J Am Ceram Soc* 2000;**83**:1428–32.

11. Pajares A, Guiberteau F, Lawn BR, Lathabai S. Hertzain contact damage in magnesia – partially stabilised zirconia. *J Am Ceram Soc* 1995;**78**(4):1083–6.
12. Latella BA, Liua T, Atanacio AJ. Effect of grain size on Hertzian contact damage in 9 mol% Ce-TZP ceramics. *J Eur Ceram Soc* 2002;**22**:1971–9.
13. Lawn BR. Indentation of ceramics with spheres: a century after hertz. *J Am Ceram Soc* 1998;**81**(8):1977–94.
14. Gaillard Y, Jiménez-Piqué E, Soldera F, Mücklich F, Anglada M. Quantification of hydrothermal degradation in zirconia by nanoindentation. *Acta Mater* 2008;**56**:4206–16.
15. Muñoz-Tabares JA, Jiménez-Piqué E, Anglada M. Subsurface evaluation of hydrothermal degradation of zirconia. *Acta Mater* 2011;**59**:473–548.
16. Oliver WC, Pharr GM. An improved technique for determining hardness and elastic modulus using load and displacement sensing indentation experiments. *J Mater Res* 1992;**7**:1564–83.
17. Gaillard Y, Jimenez-Pique E, Anglada M. Scale dependence of the Young's modulus measured by nanoindentation in columnar YSZ EB-PVD thermal barriers coatings. *Philos Magaz* 2006;**86**:5441–51.
18. Montagne A, Tromas C, Audurier V, Woirgard J. A new insight on reversible deformation and incipient plasticity during nanoindentation test in MgO. *J Mater Res* 2009;**24**:883–9.
19. Field JS, Swain MV. A simple predictive model for spherical indentation. *J Mater Res* 1993;**8**(2):297–305.
20. Herbert EG, Pharr GM, Oliver WC, Lucas BN, Hay JL. On the measurement of stress–strain curves by spherical indentation. *Thin Solid Films* 2001;**398–399**:331–5.
21. Basu S, Mosenson A, Barsoum MW. On the determination of spherical nanoindentation stress–strain curves. *J Mater Res* 2006;**21**(10):2628–37.
22. He LH, Swain M. Nanoindentaion derived stress–strain properties of dental materials. *Dent Mater* 2007;**23**:814–21.
23. Pathak S, Kalidindi SR, Klemenz C, Orlovskaya N. Analyzing indentation stress–strain response of $LaGaO_3$ single crystals using spherical indenters. *J Eur Ceram Soc* 2008;**28**:2213–20.
24. Kucheyev SO, Hamza AV, Satcher Jr JH, Worsely MA. Depth-sensing indentation of low density brittle nanoporous solids. *Acta Mater* 2009;**57**:3472–80.
25. Tabor D. Hardness of metals. Oxford: Clarendon Press; 1951.
26. Oliver WC, Pharr GM. Measurement of hardness and elastic modulus by instrumented indentation: advances in understanding and refinements to methodology. *J Mater Res* 2004;**19**:3–20.
27. Sneddon IN. The relaxation between load and penetration in the axisymmetric boussinesq problem for a punch of arbitrary profile. *Int J Eng Sci* 1965;**3**:47.
28. Johanson KL. Contact mechanics. Cambridge: Cambridge University Press; 1985.
29. ASTM C 20-00. Standard test methods for apparent porosity, water absorption, apparent specific gravity, and bulk density of burned refractory brick and shapes by boiling water.
30. Liang Y-H, Arai Y, Ozasa K, Ohashi M, Tsuchida E. Simultaneous measurement of nanoprobe indentation force and photoluminescence of InGaAs/GaAs quantum dots and its simulation. *Physica E* 2007;**36**: 1–11.
31. Linss V, Schwarzer N, Chudoba T, Karniychuk M, Richter F. Mechanical properties of a graded B–C–N sputtered coating with varying Young's modulus: deposition, theoretical modelling and nanoindentation. *Surf Coat Technol* 2005;**195**:287–97.
32. Fischer-Cripps AC. Critical review of analysis and interpretation of nanoindentation test data. *Surf Coat Technol* 2006;**200**:4153–65.
33. Moseson AJ, Basu S, Barsoum MW. Determination of the effective zero point of contact for spherical nanoindentation. *J Mater Res* 2008;**23**:204–9.
34. Dorn MT, Nickel KG. Zirconia ceramics: phase transitions and raman microspectroscopy. In: Gogotsi Y, Domnich V, editors. *High-pressure surface science and engineering*. London: IOP Publishing Ltd; 2004. p. 467–520.
35. Katagiri G, Ishida H, Ishitani A, Masaki T. Direct determination by Raman microprobe of the transformation zone size in Y_2O_3 containing tetragonal ZrO_2 polycrystals. In: Somiya S, Yamamoto N, Yanagida H, editors. *Science and technology of zirconia III*. Westerville, OH: American Ceramic Society; 1988. p. 537–44.
36. He LH, Fujisawa N, Swain M. Elastic modulus and stress–strain response of human enamel by nano-indentation. *Biomaterials* 2006;**27**(24):4388–98.
37. Rice RW. Porosity of ceramics. New York: Marcel Dekker; 1998.
38. Luo J, Steven R. Porosity-dependence of elastic moduli and hardness of 3Y-TZP ceramics. *Ceram Int* 1999;**25**:281–6.
39. Gaillard Y, Anglada M, Jimenez-Pique E. Nanoindentaion of yttria doped zirconia: effect of crystallographic structure on deformation mechanisms. *J Mater Res* 2009;**24**(3):719–27.
40. Ruhle M, Heuer AH. Phase Transformations in ZrO – containing ceramics II, the martensitic reaction in t-ZrO. In: Claussen N, Ruhle M, Heuer AH, editors. *Advances in ceramics. Science and technology of Zirconia II*, vol. 12. Columbus: The American Ceramic Society; 1984. p. 14–32.
41. Suresh A, Mayo MJ, Porter WD, Rawn CJ. Crystallite and grain-size-dependent phase transformations in yttria-doped zirconia. *J Am Ceram Soc* 2003;**86**(2):360–2.
42. Chintapalli R, Mestra A, García Marro F, Yan H, Reece M, Anglada M. Stability of nanocrystalline spark plasma sintered 3Y-TZP. *Materials* 2010;**3**(2):800–14.
43. Chen W. Model of transformation toughening in brittle material. *J Am Ceram Soc* 1991;**74**:2564–72.
44. Heuer AH, Claussen N, Keriven WM, Ruhle M. Stability of tetragonal ZrO_2 particles in ceramic matrices. *J Am Ceram Soc* 1982;**65**(12):642–50.
45. Schmauder S, Mader W, Ruhle M. Calculations of strain distributions in and around ZrO_2 inclusions. In: Claussen N, Ruhle M, Heuer AH, editors. *Advances in ceramics. Science and technology of zirconia II*, vol. 12. Columbus: The American Ceramic Society; 1984. p. 251–6.
46. Chen IW, Chiao YH. Martensitic transformations in ZrO_2 and HfO_2. An assessment of small particle experiments with metal and ceramic matrices. In: Claussen N, Ruhle M, Heuer AH, editors. *Advances in ceramics. Science and technology of zirconia II*, vol. 12. Columbus: The American Ceramic Society; 1984. p. 33–46.